Science Advances
AAAS

Manuscript Template

FRONT MATTER

Title

- Molecular Insights into the surface catalyzed secondary nucleation of Amyloid-β_{40} (Aβ40) by the peptide fragment $A\beta_{16\text{-}22}$.

Authors

[1,2]Samuel J. Bunce,† [3] Yiming Wang,† [2,4]Katie L. Stewart,[2,4]Alison E. Ashcroft, [2,4]Sheena E. Radford,* [3]Carol K. Hall,* and [1,2]Andrew J. Wilson*

Affiliations

[1]School of Chemistry, University of Leeds, Leeds LS2 9JT, U.K.
[2]Astbury Centre for Structural Molecular Biology, University of Leeds, Leeds LS2 9JT, U.K.
[3]Department of Chemical and Biomolecular Engineering, North Carolina State University, Raleigh, NC 27695-7905, U.S.A.,
[4]School of Molecular and Cellular Biology, Faculty of Biological Sciences, University of Leeds, Leeds LS2 9JT, U.K.
E-mail: s.e.radford@leeds.ac.uk E-mail: hall@ncsu.edu, E-mail: A.J.Wilson@leeds.ac.uk
† These authors contributed equally to this work

Teaser

Combined experiment and simulation reveals a structural mechanism of surface catalysed nucleation in Aβ amyloid formation

Abstract

Understanding the structural mechanism by which proteins and peptides aggregate is crucial given the role of fibrillar aggregates in debilitating amyloid diseases and bioinspired materials. Yet, this is a major challenge given assembly involves multiple heterogeneous and transient intermediates. Here, we analyze the co-aggregation of $A\beta_{40}$ and $A\beta_{16\text{-}22}$, two widely studied peptide fragments of $A\beta_{42}$ implicated in Alzheimer's disease. We demonstrate that $A\beta_{16\text{-}22}$ increases the aggregation rate of $A\beta_{40}$ through a surface catalyzed secondary nucleation mechanism. Discontinuous molecular dynamics simulations allowed aggregation to be tracked from the initial random coil monomer to the catalysis of nucleation on the fibril surface. Together, the results provide insight into how dynamic interactions between $A\beta_{40}$ monomers/oligomers on the surface of pre-formed $A\beta_{16\text{-}22}$ fibrils nucleate $A\beta_{40}$ amyloid assembly. This new understanding may facilitate development of surfaces designed to enhance or suppress secondary nucleation and hence to control the rates and products of fibril assembly.

MAIN TEXT

Introduction

Understanding the molecular mechanisms of peptide self-assembly into amyloid fibrils is of key importance in understanding pathological disease states,(*1*) as well as in designing new functional materials.(*2*) Aberrant self-assembly of monomeric peptides or proteins

into amyloid fibrils is associated with a number of degenerative conditions, notably Alzheimer's and Parkinson's disease,(*1, 3*) in which considerable evidence now implicates soluble oligomers as the primary cause of cellular damage.(*4, 5*) Identifying and characterizing the structural changes that occur during peptide assembly into amyloid fibrils is essential in the quest to develop strategies to combat disease and manufacture bespoke materials. (*1, 6*)

Peptide assembly into amyloid fibrils occurs via a complex nucleation-dependent mechanism in which subtle changes in lowly populated states can have dramatic effects on the rates and products of assembly.(*7*) Elegant work has resulted in kinetic models that are able to dissect the different contributing steps in assembly, including primary nucleation, elongation, fragmentation, and secondary nucleation.(*8-11*) Secondary nucleation is the process whereby transient binding to a fibril surface accelerates aggregation by promoting the formation of nuclei on the fibril surface. The activation energy barrier for this phase of aggregation for $A\beta_{42}$ has been shown to be enthalpic (*11*) and distinct from that of other kinetic phases of assembly. Secondary nucleation is thought to be a specific process in which the effectiveness of nucleation can depend both on the sequence and morphology of the fibril and that of the assembling monomers, although the 'rules' defining this specificity have yet to be elucidated. However, elucidating structural insights into these different steps in assembly, including the nature of early oligomeric species, is challenging, as circular dichroism (CD), infra-red (IR) and other spectroscopic techniques generally only observe population-average data for a whole system. Single molecule Förster Resonance Energy Transfer (FRET) and solid-state nuclear magnetic resonance (NMR), which have uncovered clues as to the structure of toxic versus non-toxic oligomeric species,(*12, 13*) provide information on the average properties of the different species at different times. Native ion mobility spectrometry-mass spectrometry (IMS-MS) separates ions based on shape as well as mass and charge,(*14*) and has been used to provide insights into the population, conformation and ligand-binding capability of individual peptide monomers and oligomers.(*15*) By using photo-induced cross-linking (PIC), fleeting inter/intra-peptide interactions may be trapped through covalent bond formation (to encode supramolecular connectivity).(*16*) Molecular Dynamics (MD) simulations focusing on multi-peptide systems at short time scales (<1 ms)(*17*) can help fill the gaps between population- average data and individual structures. Such simulations can provide insights into self-assembly events in molecular detail, allowing the earliest stages of aggregation to be visualized and the course of aggregation to be tracked in all-atom detail.(*18-20*)

The amyloid-β peptide (Aβ) is a major component of the extracellular plaques observed in Alzheimer's disease.(*5, 21*) Aggregation of $A\beta_{40/42}$ (Fig. 1a) into amyloid fibrils has been widely studied both *in vitro* and *in vivo*,(*22*) although numerous questions remain about its structure and role in Alzheimer's disease progression.(*1, 22*) Kinetic analysis of the sigmoid growth curves of $A\beta_{40/42}$ aggregation has enabled their assembly mechanisms to be deconvoluted into a number of microscopic steps.(*7, 10*) Assembly begins with a lag phase, during which time monomers and small amounts of oligomers persist.(*7*) Monomers then undergo a rearrangement step to form a nucleus (primary nucleation) from which fibrils can grow. Further aggregate growth occurs through pathways that include elongation (whereby a monomeric peptide adds onto the end of a growing fibril), fragmentation (fibrils break into two smaller aggregates, exponentially increasing growth-competent fibril ends), and surface catalyzed secondary nucleation (whereby nucleation is catalyzed on the fibril surface).(*23*) Using MD simulations, the energy landscape of $A\beta_{40}$

oligomer formation has also been modelled, demonstrating the different kinetic pathways that underlie the formation of pre-fibrillar and non-fibrillar oligomers.(*17*) For $A\beta_{40}$, primary nucleation has been shown to be a slower process than secondary pathways, such that surface-catalyzed secondary nucleation events dominate the growth rate of fibrils.(*10*) Under quiescent conditions, the contribution of fibril fragmentation to the growth of fibrils has been shown to be negligible.(*9*) Co-aggregation processes (i.e. where two different peptide sequences interact during aggregation but need not co-assemble) can result in more complex kinetics, due to the possibility of the sequences interacting with each other to modulate aggregation.(*24, 25*) Such a situation may occur *in vivo* wherein multiple sequences of different length of Aβ are formed.(*26*)

Here, we combine fluorescence assays, ESI-IMS-MS, and photoinduced crosslinking (PIC) experiments to study the structural mechanism of co-assembly of the peptide fragment $A\beta_{16\text{-}22}$ (Fig. 1a), which contains the "core recognition motif" KLVFF(*27*) of $A\beta_{40,}$ with the parent $A\beta_{40}$ sequence. $A\beta_{16\text{-}22}$ has been shown to form fibrils with an in-register, antiparallel orientation at neutral pH,(*28*) and has been proposed to assemble via an intermediate with out-of-register β-sheet alignment prior to reaching the final in-register fibril structure.(*29*) The rate of $A\beta_{16\text{-}22}$ aggregation is dependent on peptide concentration and ionic strength.(*29-31*) Discontinuous molecular dynamics (DMD), have also shown that the nucleation-dependent aggregation process of $A\beta_{16\text{-}22}$ proceeds from a random coil configuration to form multi-layer β-sheet fibrils, with an in-register antiparallel β-sheet orientation, in accordance with the experimental data.(*32*) Here we show, using fluorescence quenching assays, that $A\beta_{16\text{-}22}$ aggregates more rapidly than $A\beta_{40,}$ and that $A\beta_{16\text{-}22}$ fibril formation then increases the aggregation rate of $A\beta_{40}$ through a surface catalyzed, secondary nucleation mechanism, mirroring the behavior observed in kinetic analyses of $A\beta_{40/42}$ aggregation(*9, 10*) and their co-aggregation.(*24*) Using DMD simulations we also show that the preformed $A\beta_{16\text{-}22}$ fibrils increase the early-stage aggregation rate of $A\beta_{40}$, but that the monomeric $A\beta_{16\text{-}22}$ peptides do not, supporting secondary nucleation as the mechanism of enhanced $A\beta_{40}$ aggregation by $A\beta_{16\text{-}22}$. Importantly, these experimentally validated simulations portray the structural mechanism of surface catalyzed nucleation. This new understanding may pave the way to the generation of surfaces able to enhance or suppress assembly and may inform effective design of ligands that modulate therapeutically important amyloid assembly.

Results

$A\beta_{16\text{-}22}$ increases the aggregation rate of $A\beta_{40}$

To determine whether the presence of $A\beta_{16\text{-}22}$ affects the aggregation rate of $A\beta_{40}$, the peptides were synthesized or expressed recombinantly, respectively (see Experimental Methods, Supplementary Materials and Figs. S1-S2), purified and mixed in different ratios at a constant total peptide concentration of 40 μM. The rate of aggregation was then measured using the fluorescence of Thioflavin-T (ThT) (Fig. 1b, Experimental Methods and Fig. S3). Initial experiments showed the expected sigmoid increase in ThT fluorescence for $A\beta_{40}$,(*7, 10, 33*) indicating the assembly of this peptide into amyloid fibrils (Fig. 1b). Interestingly, while $A\beta_{16\text{-}22}$ formed fibrils under the conditions employed based on TEM images (Fig. 2f and Supplementary Materials, Fig. S4)), as expected,(*16*) ThT fluorescence did not increase over 12 h (Fig. 1b), indicating that the fibrils formed are either unable to bind ThT or do not enhance its fluorescence when bound; rotational immobilization of ThT is required for its fluorescent enhancement when bound to amyloid fibrils.(*34*) Other amyloid dyes (NIAD-4, Congo Red, ANS) were screened against $A\beta_{16\text{-}22}$

fibrils; however, none produced a signal with which to perform kinetic assays (data not shown). The increase in ThT signal in the peptide mixture thus reports on the aggregation rate of $A\beta_{40}$ and how this is affected by the presence of $A\beta_{16-22}$. Interestingly, the experiments in Fig. 1b show that, at constant peptide concentration of 40 μM as the molar ratio of $A\beta_{16-22}$ to $A\beta_{40}$ is increased, the apparent aggregation rate of $A\beta_{40}$ also increases. Competition between the increased rate of $A\beta_{40}$ aggregation as $A\beta_{16-22}$ concentration increases and the decreased rate of aggregation of $A\beta_{40}$ as its concentration correspondingly decreases results in maximal apparent rate enhancement at a 1:1 molar ratio of the two peptides (Fig. 1b). We accounted for this effect by measuring, in parallel, the t_{50} of aggregation of $A\beta_{40}$ alone at each concentration and comparing the t_{50} values with and without $A\beta_{16-22}$ added (See Fig. S3). These data show that the effect saturates as would be expected for secondary nucleation events involving binding to the fibril surface.

In order to characterize the extent to which $A\beta_{40}$ aggregation is accelerated by the presence of $A\beta_{16-22}$, the half-time ($t_{1/2}$, the time at which the growth curve reaches 50% amplitude) was calculated for each peptide mixture and normalized to the half time for the equivalent concentration of $A\beta_{40}$ alone (Fig. S3). The results revealed a dramatic, and titratable, effect of the presence of $A\beta_{16-22}$ on the aggregation rate of $A\beta_{40}$, demonstrating an interaction between the two peptides that accelerates the rate of assembly.

$A\beta_{16-22}$ aggregates more rapidly than $A\beta_{40}$ and is unaffected by the presence of $A\beta_{40}$

As the assembly kinetics of $A\beta_{16-22}$ could not be measured using any of the amyloid dyes surveyed at the concentrations employed here, a fluorescence quenching assay was developed to determine whether $A\beta_{16-22}$ aggregates more or less rapidly than $A\beta_{40}$ (Fig. 2a). Similar assays have been used previously to monitor the aggregation rates of $A\beta_{40}$ and $A\beta_{42}$,(*35*) with fluorescence quenching reporting on labelled monomers coming into mutual proximity as oligomers (or fibrils) form. For these assays $A\beta_{16-22}$ *N*-terminally labelled with tetramethylrhodamine (TAMRA) was synthesized, including a 6-aminohexanoic acid linker (Ahx) to limit disruption to the native fibril structure that might arise due to the bulky fluorophore (TAMRA-Ahx-$A\beta_{16-22}$) (Supplementary Materials and Figs. S1 and S4). When incubated in isolation, a 5% (w/w) TAMRA-Ahx-$A\beta_{16-22}$: 95% $A\beta_{16-22}$ mixture (20 μM) resulted in a rapid decrease in fluorescence intensity followed by a slower phase that plateaued after 1 h (Fig. 2b). In the presence of $A\beta_{40}$ (1:1 (mol/mol) ratio, 40 μM total peptide concentration, and 2% (v/v) DMSO), no difference in the rate of fluorescence decrease was observed, indicating that the presence of $A\beta_{40}$ has no effect on $A\beta_{16-22}$ aggregation (Fig. 2c). Analysis of these samples by negative stain TEM showed the presence of fibrils after only 5 mins (Fig. 2f). Sedimentation of the mixed system by centrifugation after 1 h demonstrated that $A\beta_{40}$ was present mainly in the supernatant (Figs. 2d, e). These results demonstrate that $A\beta_{16-22}$ aggregates rapidly to form amyloid-like fibrils while $A\beta_{40}$ remains soluble as monomers/oligomers. Thus, although the rate of $A\beta_{40}$ aggregation is increased by the presence of $A\beta_{16-22}$, limited or no co-assembly between the two peptides into fibrils was observed. By contrast, $A\beta_{16-22}$ aggregation is unaffected by the presence of $A\beta_{40}$. $A\beta_{40}$ fibrils have been shown to adopt a parallel in register structure involving the majority of the polypeptide backbone (*21, 36*) whilst $A\beta_{16-22}$ has been shown to form an anti-parallel β-stranded amyloid structure.(*28, 29*) This structural incompatibility could account for the absence of co-assembly sincesuch a structure would be less stable compared with homomeric assemblies. Furthermore, the more rapid fibril assembly of $A\beta_{16-22}$ in comparison to $A\beta_{40}$ disfavors co-assembly on kinetic grounds.

Monomeric $A\beta_{16-22}$ can interact with monomeric and oligomeric $A\beta_{40}$ through the self-recognition motif KLVFF

To determine whether $A\beta_{16-22}$ and $A\beta_{40}$ interact transiently in the early stages of assembly, native electrospray ionization (ESI) linked to ion mobility mass spectrometry (IMS-MS) was performed (see Experimental Methods). This soft ionization technique has been used to identify and structurally characterize amyloid oligomers formed from several different proteins and peptides.(*14, 15*) Under the conditions used here, ESI-IMS-MS immediately following mixing revealed $A\beta_{40}$ co-populates a number of oligomers, ranging from monomers to pentamers (Fig. 3b (white), see also Table S1), consistent with previous results. (*33*) When incubated with $A\beta_{16-22}$, heteromolecular oligomers were observed (Fig. 3b (light blue)), along with homomolecular oligomers of $A\beta_{40}$ (Fig. 3a, (white)). Notably $A\beta_{16-22}$ homomolecular oligomers were not observed. The heteromolecular oligomers correspond to multiple $A\beta_{16-22}$ monomers bound to either an $A\beta_{40}$ monomer or dimer (Table S1). Collision cross-section (CCS) estimations from the ESI-IMS-MS analysis of the $A\beta_{40}$ species in the presence or absence of $A\beta_{16-22}$ indicate no significant difference in the gas phase cross-section of $A\beta_{40}$, implying that a conformational change in monomer or oligomer structure is unlikely to be the provenance for the $A\beta_{16-22}$ driven increase in $A\beta_{40}$ aggregation rate (Fig. S5). Despite attempts to capture the interaction experimentally by PIC using a diazirine labelled $A\beta_{16-22}$ ($A\beta^*_{16-22}$, see Supplementary Materials for synthesis, Scheme S1 and Fig. S1), the site of interaction could not be verified (Figs. S6 and Table S2), likely due to the low percentage of any heterodimers present (as assessed by total ion count, 1.0 ± 0.5%) and the lower solution concentration of $A\beta_{16-22}$ arising as a consequence of its rapid aggregation.

To assess further the nature of the interactions between $A\beta_{16-22}$ and $A\beta_{40}$, discontinuous molecular dynamics (DMD) simulations were performed (see Experimental Methods). To evaluate the role of interactions between $A\beta_{40}$ and $A\beta_{16-22}$ monomers (covered in this section), it was first necessary to perform DMD simulations on the aggregation of $A\beta_{40}$ alone (Fig. 1c), and then a 1:1 mixture of the $A\beta_{16-22}$ and $A\beta_{40}$ peptide sequences at $C_{peptide}$ = 5 mM (Fig. 3c). These co-aggregation simulations starting from monomeric peptides are further discussed in the course of our analyses to rule out co-assembly (see later), then we describe DMD analyses on the effect of $A\beta_{16-22}$ fibrils on $A\beta_{40}$ aggregation (see later). Simulations performed on six monomers of $A\beta_{40}$ (Fig. 1c) showed that the initially unstructured peptides assemble and adopt a metastable oligomer structure by 104 μs (Fig. 1c); this structure comprises antiparallel intramolecular β-strands linked by disordered regions assembled into antiparallel intermolecular sheets with β-strands stacked perpendicular to the long axis. During this oligomerization stage, the peptide conformation is similar to that observed by Zhang *et al.* (16,(*37*) As the simulation proceeds, this oligomer loses some β-sheet content (t = 230 μs, Fig. 1c). By the end of the simulation (621 μs), peptides in oligomers undergo structural rearrangement from antiparallel β-strand conformations to the parallel β-sheet conformation observed for $A\beta_{40}$ fibrils (Fig. 1c).(*37*) Interestingly, simulations of the peptide mixtures did not show an accelerating effect of $A\beta_{16-22}$ monomers on the aggregation rate of $A\beta_{40}$ (see Fig. 3c and later). However, interactions between the two peptides were observed, consistent with the ESI-MS results in Fig. 3. From the DMD data, an energy contact map between the monomeric $A\beta_{16-22}$ and $A\beta_{40}$ peptides was calculated (Fig. 3d). The contact map indicated that $A\beta_{16-22}$, specifically residues 18-20 (VFF) interact strongly with residues 19-21 and 32-35 of $A\beta_{40}$ (FFA and IGLM, respectively), consistent with experimental data previously reported, which indicates KLVFF is a "self-recognition element".(*27*) Such an interaction between

237 $A\beta_{16-22}$ and $A\beta_{40}$ oligomers, however, does not result in an acceleration of aggregation
238 (Fig. 3c) implying these mixed and low-abundance oligomers represent transient species
239 that do not affect the rate of assembly (Fig. 3e).

240 **$A\beta_{16-22}$ fibrils have a larger effect on the aggregation rate of $A\beta_{40}$ than $A\beta_{16-22}$**
241 **monomer**

242 To determine whether rapidly formed $A\beta_{16-22}$ fibrils are the causative agents of the
243 enhanced rate of $A\beta_{40}$ aggregation in the mixed samples (Fig. 1b), the effect of pre-formed
244 $A\beta_{16-22}$ fibrils on $A\beta_{40}$ aggregation was assessed. These experiments (Fig. 4a) showed that
245 the presence of $A\beta_{16-22}$ fibrils increases the rate of aggregation of $A\beta_{40}$ in a fibril
246 concentration-dependent manner (Fig. 4a) and addition of $A\beta_{16-22}$ fibrils had a larger effect
247 on aggregation rate compared with the addition of monomeric (i.e. taken straight from a
248 DMSO stock) $A\beta_{16-22}$ (Fig. 4b). This suggests that aggregation is enhanced either by cross-
249 seeding (i.e. by $A\beta_{40}$ adding directly to the ends of $A\beta_{16-22}$ fibrils) or by secondary
250 nucleation of $A\beta_{40}$ on the $A\beta_{16-22}$ fibril surface (Fig. 4e). Sonication of fibrils fragments
251 them, leading to a higher concentration of fibril ends. Hence should elongation dominate
252 the rate of fibril formation, sonication should dramatically increase the rate of fibril
253 growth. Comparison of the effects of unsonicated fibrils (fewer ends) with the same fibrils
254 fragmented by sonication (Fig. 4c, see Supplementary Materials, Fig. S4 for TEM
255 analyses) indicated that elongation was not dominant (Fig. 4c), since the average $t_{1/2}$ for
256 sonicated fibrils (6.2 ± 1.0 h) is similar to that of its unfragmented counterpart (7.2 ± 0.7
257 h). Together, the results demonstrate that the presence of rapidly formed $A\beta_{16-22}$ fibrils
258 enhances aggregation of $A\beta_{40}$ in peptide mixtures by secondary nucleation, despite the
259 presence of small amounts of mixed oligomers (as demonstrated by the ESI-IMS-MS
260 experiments).

261 DMD simulations of the aggregation of six $A\beta_{40}$ peptides were also performed in the
262 presence of pre-formed $A\beta_{16-22}$ fibrils of different sizes (two, three and four β-sheets) at a
263 $A\beta_{40}$ concentration of 1 mM to model the dynamic process of the secondary nucleation
264 event. The results (Fig. 4d) showed that the largest $A\beta_{16-22}$ fibril (i.e. four β-sheets, green
265 trace in Fig. 4d) led to the largest increase in the rate of β-sheet formation by $A\beta_{40}$. Given
266 that the presence of $A\beta_{16-22}$ monomers had no observable effect on $A\beta_{40}$ assembly (Fig.
267 3c), these simulations are thus qualitatively concordant with the experimental findings that
268 the fibrillar structure of $A\beta_{16-22}$ is the dominant influence on the aggregation rate of $A\beta_{40}$.
269 Such behavior is consistent with that observed for $A\beta_{40/42}$ co-aggregation for which a
270 kinetic model has been established.(*24*)

271 **$A\beta_{40}$ and $A\beta_{16-22}$ form distinct homomolecular fibrils**

272 The peptide composition of the final fibril structure(s) represents a further means to
273 discern the difference between surface catalyzed secondary nucleation and co-assembly
274 exploiting fibril ends. A surface catalyzed mechanism would most likely produce homo-
275 molecular fibrils of $A\beta_{40}$, as once they have formed on the $A\beta_{16-22}$ fibril surface, the $A\beta_{40}$
276 nuclei would dissociate and form pure $A\beta_{40}$ fibrils. In contrast, co-assembly involving
277 fibril ends should result in mixed fibrils, in which $A\beta_{16-22}$ seeds are segmentally separated
278 from fibril regions containing $A\beta_{40}$ monomers.

279 Negative stain TEM images taken at the end of the aggregation reaction showed $A\beta_{40}$
280 fibrils with similar gross morphology when incubated in isolation or co-aggregated with

281 $A\beta_{16-22}$ (Fig. 5a,b). Similarly, quantitation of ThT fluorescence at the end-point of
282 aggregation in mixed samples and of the same concentration of $A\beta_{40}$ incubated alone were
283 indistinguishable (Fig. S3), supporting the hypothesis that homomolecular $A\beta_{40}$ fibrils are
284 formed at the end of the assembly reaction. Finally, PIC was used to explore whether
285 homo- or heteromolecular fibrils had formed (Experimental Methods, (Fig. 5c)). To
286 perform PIC experiments, a diazirine label was placed on F20 of $A\beta_{16-22}$ ($A\beta^*_{16-22}$).(*16*)
287 Control experiments demonstrated that $A\beta^*_{16-22}$ has a similar effect on the rate of $A\beta_{40}$
288 aggregation as its unmodified counterpart (Fig. S3). PIC experiments performed 5 mins
289 and 24 hours after initiating assembly failed to detect crosslinks between $A\beta^*_{16-22}$ and
290 $A\beta_{40}$ (Figs. 5c, S6, and Table S2). Instead, all identifiable cross-links were consistent with
291 inter/intramolecular $A\beta^*_{16-22}$ or solvent adducts, as previously identified in $A\beta^*_{16-22}$-
292 containing fibrils by Preston and co-workers(*16*), indicating that co-assembly into fibrils is
293 either very rare and cannot be detected despite the sensitivity of ESI-MS, or does not
294 occur.

295 To provide a molecular image of co-assembly, we further analyzed the DMD simulations
296 in which six $A\beta_{40}$ and six $A\beta_{16-22}$ monomers were mixed and their aggregation behavior
297 was monitored versus time at $C_{peptide}$ = 5 mM (Fig. 5d). The simulations showed that in the
298 early stages of assembly (t = 0.6 μs) a mixture of monomeric and oligomeric $A\beta_{40}$ was
299 present. As the simulation progressed (t = 57 μs), all $A\beta_{40}$ peptides coalesced into one β-
300 sheet rich oligomer, with $A\beta_{16-22}$ intercalated within the structure. Throughout the
301 simulation, monomeric $A\beta_{16-22}$ was observed to bind transiently to other monomeric $A\beta_{16-}$
302 $_{22}$ peptides or the KLVFF motif of $A\beta_{40}$, in accordance with the data presented above.
303 Finally, at the end of the simulation (t = 202 μs) the peptides form distinct oligomeric
304 domains with $A\beta_{40}$ and $A\beta_{16-22}$ forming separate sheets.

305 **$A\beta_{40}$ oligomer dynamics on the surface of $A\beta_{16-22}$ fibrils**

306 To obtain a molecular image of the process of secondary nucleation, DMD simulations
307 were performed in which six $A\beta_{40}$ monomers were mixed with preformed fibrils of $A\beta_{16-22}$
308 at $C_{A\beta40}$ = 5 mM (Fig. 6a). At the early stage of the simulation (t = 0.29 μs), three $A\beta_{40}$
309 peptides were present in an oligomer, one other $A\beta_{40}$ peptide was associated at the end of
310 the fibril and the remaining two $A\beta_{40}$ peptides are elongated across the fibril surface. At
311 this stage (t = 0.29 μs), the $A\beta_{40}$ peptides in the oligomer and on the surface were observed
312 to adopt a predominantly random coil conformation with small amounts of β-strand
313 structure (note that an elongated monomeric structure was also observed in simulations
314 performed by Barz *et al*.(*19*) in exploring the secondary nucleation of $A\beta_{42}$ on the surface
315 of $A\beta_{11-42}$) . The β-sheets were next observed to act as templates for peptides present in a
316 random coil conformation (1.93 μs) and to pull them more fully to the fibril surface. Thus,
317 as the simulation progressed, the $A\beta_{40}$ peptides remaining in solution were recruited by
318 those on the fibril surface. Once the oligomer became fully associated with the fibril
319 surface, the amount of β-sheet structure in the surface-associated oligomer increased (t =
320 7.7 μs); antiparallel β-strands formed *via* inter and intramolecular hydrogen-bonding
321 leading to sheet formation consistent with the early stages observed in the simulations
322 performed for $A\beta_{40}$ alone (Fig. 1c, t = 104 μs). Finally, the surface-associated $A\beta_{40}$
323 peptides were joined in an ordered oligomer (t = 29.0 and 77.7 μs). Related "bind and re-
324 organize" processes for secondary nucleation were observed in simulations performed by
325 Schwierz *et al*. using $A\beta_{9-40}$ as a model.(*38*) As noted above, $A\beta_{40}$ peptides attached to
326 both the lateral surface and to the end of the $A\beta_{16-22}$ fibril during the simulation, with the
327 $A\beta_{40}$ C-terminal region attaching more frequently to the lateral surface of the fibril than to

the fibril ends at C = 5mM (Fig. S7). To assess the consistency of the results, the simulation was repeated three times; two of the three independent runs gave results similar to those described above, whilst for the final run, a greater number of associations to the fibril end were observed. Collectively, these results provide molecular images of surface catalyzed nucleation in which a random coil peptide is catalytically converted into a β-sheet fibrillar structure on a fibril surface.

Discussion

In this work we used ESI-MS, PIC and DMD to study the co-assembly mechanism of $A\beta_{16-22}$ and $A\beta_{40}$ into amyloid, demonstrating the power of using integrated approaches to study structural determinants of molecular assembly processes. We show that mixed $A\beta_{16-22}/A\beta_{40}$ heteromeric oligomers form, but that these are transient, lowly populated (~ 1%) and do not significantly affect the rate of aggregation. In contrast $A\beta_{16-22}$ has a high propensity to self-associate into homomolecular fibrils and these fibrils accelerate $A\beta_{40}$ assembly by monomer/oligomer interactions through secondary nucleation at the fibril surface. Recent modelling of amyloid assembly kinetics has revealed the importance of primary nucleation, secondary nucleation and fibril elongation in fibril growth mechanisms.(*7, 10, 39*) Notably, a kinetic model has been described for the co-aggregation of $A\beta_{40/42}$.(*24*) The experimental data presented here for co-aggregation of $A\beta_{16-22}$ and $A\beta_{40}$ qualitatively agree with this model, whilst our DMD simulations illustrate that whilst all primary/secondary nucleation and elongation processes occur simultaneously, secondary nucleation is the dominant process in $A\beta_{40}$ fibril formation kinetics during co-assembly with $A\beta_{16-22}$, which is consistent with the findings for the self-assembly mechanism of $A\beta_{40}$ observed previously.(*9, 10, 24*) Moreover, $A\beta_{40}$ assembly intermediates on the surface of $A\beta_{16-22}$ fibrils resemble those formed spontaneously in solution for $A\beta_{40}$ alone, implying that the fibril surface catalyzes the assembly reaction without modifying the molecular mechanism, at least for the simulations performed here. Whether or not this holds for other sequences and co-assembly reactions will require further exploration notably, which features both of a fibril and the assembling monomer determine compatibility with secondary nucleation from a fibril surface.

Overall, the current study thus serves to emphasize the dramatic differences in aggregation behavior that are observed during co-aggregation compared to homomolecular self-assembly and underscores the need to employ multiple methods to understand aggregation mechanisms in molecular detail. Significant current interest centers on characterizing distinct molecular steps leading to amyloid fibril formation, with secondary nucleation considered as playing a key role in causing toxicity.(*11, 40*) Recently, kinetic analyses have been augmented by mapping the free-energy landscapes defining different microscopic phases in the aggregation pathway,(*11*) providing insight to facilitate development of strategies that modulate the thermodynamically distinct surface-monomer interactions characteristic of secondary nucleation. However, to design therapeutically useful modulators of amyloid aggregation requires that this understanding is complemented with structural insights of the molecular recognition between fibrils and monomers, set within the context of other interactions occurring during aggregation (e.g. monomer-nuclei interactions). We have shown here that $A\beta_{40}$ monomers and oligomers dock onto the fibril surface, which catalyzes assembly of antiparallel strand formation in close *situ* to the parent $A\beta_{16-22}$ fiber. Whether this is the end-point product or further re-organization is required to generate the final amyloid structure, requires further study (longer simulation time). Interestingly in this context, metastable amyloid structures have been observed for the the Iowa mutant of $A\beta_{40}$ using solid state NMR, in which

antiparallel fibrils were observed as trapped intermediates in the assembly process to the final all-parallel fibril structure.(*41*)

Together the results demonstrate that kinetic analyses and theory together with molecular dynamics provide a powerful arsenal and capability to visualize secondary nucleation in structural and kinetic detail. Such approaches may allow informed targeting of this process to either prevent or accelerate secondary nucleation for therapeutic purposes and peptide materials assembly. Co-aggregation adds an additional layer of complexity in understanding molecular assembly, yet represents an opportunity to manipulate these supramolecular assembly processes, as demonstrated here for the model system involving $A\beta_{16\text{-}22}$ and $A\beta_{40}$. Evidently $A\beta_{40}$ shows propensity to aggregate *via* secondary nucleation from its own fibril surface or that of other peptide sequences, as shown here for fibrils of $A\beta_{16\text{-}22}$. Hence this work begins to address the molecular recognition events required for secondary nucleation to occur on a fibril surface, and may inform strategies to modulate the aggregation of $A\beta_{40}$ under conditions in which secondary nucleation dominates fibril growth.

Materials and Methods

Synthesis of *N*-Fmoc TFMD-Phe and amyloid-β peptides

N-Fmoc TFMD-Phe was synthesized using the method described by Smith *et al*. and further minor changes in protecting group (Scheme S1).(*42*) $A\beta_{16\text{-}22}$, TAMRA-Ahx-$A\beta_{16\text{-}22}$ and $A\beta^*_{16\text{-}22}$ were synthesized via both automated and manual solid-phase peptide synthesis and dissolved into dimethylsulfoxide (DMSO) stock solutions prior to use (Fig. S1). $A\beta_{40}$ was synthesized recombinantly using the method of Walsh and co-workers and modifications by Stewart and co-workers.(*43, 44*) To ensure that $A\beta_{40}$ was monomeric prior to use, the peptide was purified by size exclusion chromatography, lyophilized and stored at -4 °C (Fig. S2).

Thioflavin T fluorescence assays

Samples were prepared in a 96-well non-binding plate (Corning Costar 3881, Corning Life Sciences, Amsterdam, The Netherlands) sealed with clear sealing film (BMG Labtech, Aylesbury, Bucks, UK) and were incubated in a FLUOstar OPTIMA plate reader (BMG Labtech, Aylesbury, Bucks, UK) for 20 hours at 37 °C without agitation. Samples had a volume of 95 µL containing 10 µM ThT in 100 mM ammonium bicarbonate, pH 7.4 and a final concentration of 1% (v/v) DMSO. For seeding experiments, $A\beta_{16\text{-}22}$ was incubated at 50 µM for at least 24 hours in the same buffer as described above with the presence of fibrils confirmed by Transmission Electron Microscopy (TEM, described below). Prior to the assay, the fibrils were probe sonicated for 5 s at 22% amplitude to generate "seeds". The ThT experiments used excitation and emission filters of 430 and 485 nm. Each ThT experiment shown was repeated in independent assays on three different occasions with the traces shown in this work being representative of all repeats.

Transmission Electron Microscopy

TEM images were taken at the end of each experiment by removing 5 μL from the necessary well and incubating this sample on carbon-formvar grids for 30 s prior to staining with 2% (w/v) uranyl acetate solution for an additional 30 s as described by Preston et al.[27] Images were taken on a JEM-1400 (JEOL Ltd., Tokyo, Japan) or a Technai F12 transmission electron microscope. Images were taken on a JEM-1400 (JEOL Ltd., Toyko, Japan) or an Tecnai T12 (FEI, Oregon, USA) transmission electron microscopes. Images were taken using either a ATM CCD camera or a Gatan Ultrascan 1000 XP (994) CCD camera (JEM-1400) or an Ultrascan 100XP (994) CCD camera (Tecnai F12). Once taken, images were processed using ImageJ (NIH).

General Sedimentation Protocol

Samples were taken at the desired time point and centrifuged (20 mins, 14,000 g, 4 °C). Each sample was then separated into pellet and supernatant fractions, lyophilised overnight and disaggregated in hexafluoroisopropanol (HFIP) for at least 2 hours. The HFIP was removed under a stream of N_2 and the peptides were taken up in DMSO prior to analysis by high-resolution mass spectrometry (Bruker HCT ion-trap MS).

Fluorescence Quenching Assays

Wild type $A\beta_{16\text{-}22}$ was spiked with 5% w/w TAMRA-Ahx-$A\beta_{16\text{-}22}$ and incubated either in isolation or at a 1:1 ratio with $A\beta_{40}$ (total peptide concentration 40 μM) in 100 mM ammonium bicarbonate buffer, pH 7.4 with a final concentration of 2% (v/v) of DMSO. Samples were placed in quartz cuvettes and analysed using a temperature controlled fluorimeter at 37 °C. Time points were taken every 30 s for the duration of the experiment and TEM images (as described above) were taken at the end of each experiment to ensure the presence of fibrils. The TAMRA fluorophore was excited at 520 nm and emission recorded at 600 nm to reduce the inner filter effect.

ESI-IMS-MS analysis

All samples were prepared as described above and left to incubate at 37 °C without agitation for 5 mins. A Synapt HDMS quadrupole time-of-flight mass spectrometer (Micromass UK Ltd., Waters Corpn., Manchester, UK), equipped with a Triversa NanoMate (Advion Biosciences, Ithaca, NY, USA) automated nano-ESI interface was used in this study. The instrument has a travelling-wave IMS device situated in-between the quadrupole and the time-of-flight analysers, as described in detail elsewhere. Samples were analysed by positive ionization nanoESI (nESI) with a capillary voltage of 1.4 kV and a nitrogen nebulizing gas pressure of 0.8 psi. The following instrumental parameters were set: cone voltage 60 V; source temperature 60 °C; backing pressure 4.7 mbar; ramped travelling speed 7-20 V; travelling wave speed 400 m s^{-1}; IMS nitrogen gas flow 20 mL min^{-1}; IMS cell pressure 0.55 mbar. The m/z scale was calibrated using aq. CsI cluster ions. Collision cross-section (CCS) measurements were estimated by use of a calibration obtained by analysis of denatured proteins (cytochrome c, ubiquitin, alcohol dehydrogenase) and peptides (tryptic digests of alcohol dehydrogenase and cytochrome c) with known CCSs obtained elsewhere from drift tube ion mobility measurements.(*15, 33*) Data were processed by use of MassLynx v4.1 and Driftscope softwave supplied with the mass spectrometer.

Photo-induced covalent cross-linking (PIC)

A 1:1 ratio of $A\beta_{16-22}/A\beta^*_{16-22}$ or $A\beta^*_{16-22}/A\beta_{40}$ (40 μM total peptide concentration) in 100 mM ammonium bicarbonate buffer, pH 7.4 with a final concentration of 1% (v/v) DMSO was incubated in eppendorf tubes for either 5 mins or 24 h. Samples were then irradiated for 30 s using a home built LED lamp at 365 nm, then removed, lyophilized overnight, taken up in hexafluoroisopropanol (HFIP) for at least 2 hours and vortexed to ensure any aggregates were disrupted. The HFIP was then removed under a stream of N_2 and the sample re-suspended in 50/50 $MeCN/H_2O$ (v/v) + 0.05% formic acid to a final concentration of ~40 μM. Any cross-links were then analysed using the method previously described and the ESI-IMS-MS system as described above.(*16*)

Discontinuous Molecular Dynamics and PRIME20 Force Field

The simulation approach applied in this work is discontinuous molecular dynamics (DMD), a fast alternative to traditional molecular dynamics, in combination with the PRIME20 force field, a four-bead-per-residue coarse-grained protein model developed in the Hall group.(*45*) In the PRIME20 model, each of the 20 different amino acids contains three backbone spheres NH, $C_\alpha H$, CO and one sidechain sphere R with a distinct hard sphere diameter (effective van der Waals radius) and distinct sidechain-to-backbone distances (R-CαH, R-NH, R-CO). The backbone hydrogen bonding interaction is modelled as a directional square well potential. In the original PRIME20 force field, the potential function between any two sidechain beads on the twenty different amino acids (except glycine) is modelled as a single well potential, containing 210 different square well widths and 19 different square well depths using the 5.5Å heavy atom criteria. In this work, we follow Cheon's approach to apply a double square well potential instead of the single square well for sidechain-sidechain interaction.(*46*) All the other non-bonded interactions are modelled as hard sphere interactions. A detailed description of the derivation of the geometric and energetic parameters of the PRIME20 model is given in our earlier work.(*47*)

Simulation Procedure

DMD/PRIME20 simulations were performed on the following systems: 1. six $A\beta_{40}$ monomeric peptides; 2. six monomeric $A\beta_{40}$ peptides with six monomeric $A\beta_{16-22}$ peptides; 3. six $A\beta_{40}$ monomeric peptides in the presence of pre-formed two, three and four β-sheet $A\beta_{16-22}$ protofilaments, respectively. The 2, 3 and 4 β-sheet $A\beta_{16-22}$ protofilaments contain 21, 42 and 71 peptides, respectively. Each simulation is performed at two different total peptide concentrations (1 and 5 mM). Similar seeding simulations have been performed in previous works.(*46*) The simulations are performed in the canonical ensemble (fixed number of particles, volume and temperature). The reduced temperature is defined to be $T^* = k_B T/\varepsilon_{HB}$, where the hydrogen bonding energy, ε_{HB}=12.47kJ/mol. The reduced temperature is related to real temperature by using the equation $T/K = 2288.46\ T^* - 115.79$. The reduced temperature T^* is chosen to be 0.20, which corresponds to a real temperature of 342K. The system is maintained at a constant temperature by applying the Andersen thermostat. We have performed three to ten independent runs for each system.

Additional Data

All data needed to evaluate the conclusions in the paper are present in the paper and/or the Supplementary Materials. Additional data available from authors upon request

H2: Supplementary Materials

References and Notes

1. T. P. J. Knowles, M. Vendruscolo, C. M. Dobson, The amyloid state and its association with protein misfolding diseases. *Nat. Rev. Mol. Cell Biol.* **15**, 384-396 (2014).
2. L. Adler-Abramovich, E. Gazit, The physical properties of supramolecular peptide assemblies: from building block association to technological applications. *Chem. Soc. Rev.* **43**, 6881-6893 (2014).
3. M. G. Iadanza, M. P. Jackson, E. W. Hewitt, N. A. Ranson, S. Ranson, A New Era for Understanding Amyloid Structures and Disease. *Nat. Rev. Mol. Cell Biol.* **19**, 755-773 (2018).
4. R. Kayed *et al.*, Common structure of soluble amyloid oligomers implies common mechanism of pathogenesis. *Science* **300**, 486-489 (2003).
5. C. Haass, D. J. Selkoe, Soluble protein oligomers in neurodegeneration: lessons from the Alzheimer's amyloid beta-peptide. *Nat. Rev. Mol. Cell Biol.* **8**, 101-112 (2007).
6. D. Eisenberg, M. Jucker, The amyloid state of proteins in human diseases. *Cell* **148**, 1188-1203 (2012).
7. S. I. A. Cohen, M. Vendruscolo, C. M. Dobson, T. P. J. Knowles, From macroscopic measurements to microscopic mechanisms of protein aggregation. *J. Mol. Biol.* **421**, 160-171 (2012).
8. W.-F. Xue, S. W. Homans, S. E. Radford, Systematic analysis of nucleation-dependent polymerization reveals new insights into the mechanism of amyloid self-assembly. *Proc. Natl. Acad. Sci. U. S. A.* **105**, 8926-8931 (2008).
9. S. I. A. Cohen *et al.*, Proliferation of amyloid-β42 aggregates occurs through a secondary nucleation mechanism. *Proc. Natl. Acad. Sci. U. S. A.* **110**, 9758-9763 (2013).
10. G. Meisl *et al.*, Differences in nucleation behavior underlie the contrasting aggregation kinetics of the Aβ40 and Aβ42 peptides. *Proc. Natl. Acad. Sci. U. S. A.* **111**, 9384-9389 (2014).

554 11. S. I. A. Cohen *et al.*, Distinct thermodynamic signatures of oligomer generation in the
555 aggregation of the amyloid-β peptide. *Nat. Chem.* **10**, 523-531 (2018).
556 12. G. Fusco *et al.*, Structural basis of membrane disruption and cellular toxicity by α-
557 synuclein oligomers. *Science* **358**, 1440-1443 (2017).
558 13. J. A. Varela *et al.*, Optical Structural Analysis of Individual α-Synuclein Oligomers.
559 *Angew. Chem. Int. Ed.* **57**, 4886-4890 (2018).
560 14. S. L. Bernstein *et al.*, Amyloid-β protein oligomerization and the importance of tetramers
561 and dodecamers in the aetiology of Alzheimer's disease. *Nat. Chem.* **1**, 326-331 (2009).
562 15. L. M. Young, L.-H. Tu, D. P. Raleigh, A. E. Ashcroft, S. E. Radford, Understanding co-
563 polymerization in amyloid formation by direct observation of mixed oligomers. *Chem.*
564 *Sci.* **8**, 5030-5040 (2017).
565 16. G. W. Preston, S. E. Radford, A. E. Ashcroft, A. J. Wilson, Covalent Cross-Linking
566 within Supramolecular Peptide Structures. *Anal. Chem.* **84**, 6790-6797 (2012).
567 17. W. Zheng, M.-Y. Tsai, M. Chen, P. G. Wolynes, Exploring the aggregation free energy
568 landscape of the amyloid-β protein (1-40). *Proc. Natl. Acad. Sci. U. S. A.* **113**, 11835-
569 11840 (2016).
570 18. T. Gurry, C. M. Stultz, Mechanism of Amyloid - β Fibril Elongation. *Biochemistry* **53**,
571 6981-6991 (2014).
572 19. B. Barz, B. Strodel, Understanding Amyloid-β Oligomerization at the Molecular Level:
573 The Role of the Fibril Surface. *Chem. Eur. J.* **22**, 8768-8772 (2016).
574 20. B. Barz, Q. Liao, B. Strodel, Pathways of Amyloid-β Aggregation Depend on Oligomer
575 Shape. *J. Am. Chem. Soc.* **140**, 319-327 (2018).
576 21. W. Qiang, W.-M. Yau, J.-X. Lu, J. Collinge, R. Tycko, Structural variation in amyloid-β
577 fibrils from Alzheimer's disease clinical subtypes. *Nature* **541**, 217-221 (2017).
578 22. B. De Strooper, E. Karran, The Cellular Phase of Alzheimer's Disease. *Cell* **164**, 603-615
579 (2016).
580 23. M. Törnquist *et al.*, Secondary nucleation in amyloid formation. *Chem. Commun.* **54**,
581 8667-8684 (2018).
582 24. R. Cukalevski *et al.*, The Aβ40 and Aβ42 peptides self-assemble into separate
583 homomolecular fibrils in binary mixtures but cross-react during primary nucleation.
584 *Chem. Sci.* **6**, 4215-4233 (2015).
585 25. C. J. Sarell, P. G. Stockley, S. E. Radford, Assessing the causes and consequences of co-
586 polymerization in amyloid formation. *Prion* **7**, 359-368 (2013).
587 26. M. Jucker, L. C. Walker, Self-propagation of pathogenic protein aggregates in
588 neurodegenerative diseases. *Nature* **501**, 45-51 (2013).
589 27. L. O. Tjernberg *et al.*, Arrest of β-Amyloid by a Pentapeptide Ligand. *J. Biol. Chem.* **271**,
590 8545-8549 (1996).
591 28. J. J. Balbach *et al.*, Amyloid fibril formation by A$\beta_{16\text{-}22}$, a seven-residue fragment of the
592 Alzheimer's β-amyloid peptide, and structural characterization by solid state NMR.
593 *Biochemistry* **39**, 13748-13759 (2000).
594 29. M. C. Hsieh, C. Liang, A. K. Mehta, D. G. Lynn, M. A. Grover, Multistep Conformation
595 Selection in Amyloid Assembly. *J. Am. Chem. Soc.* **139**, 17007-17010 (2017).
596 30. S. A. Petty, S. M. Decatur, Experimental evidence for the reorganization of β-strands
597 within aggregates of the Aβ(16-22) peptide. *J. Am. Chem. Soc.* **127**, 13488-13489 (2005).
598 31. F. T. Senguen *et al.*, Probing aromatic, hydrophobic, and steric effects on the self-
599 assembly of an amyloid-β fragment peptide. *Mol. BioSys.* **7**, 486-496 (2011).
600 32. M. Cheon, I. Chang, Carol K. Hall, Spontaneous Formation of Twisted Aβ16-22 Fibrils in
601 Large-Scale Molecular-Dynamics Simulations. *Biophys. J.* **101**, 2493-2501 (2011).
602 33. L. M. Young *et al.*, Insights into the consequences of co-polymerisation in the early stages
603 of IAPP and Aβ assembly from mass spectrometry. *Analyst* **20**, 6990-6999 (2015).

34. M. Biancalana, S. Koide, Molecular mechanism of Thioflavin-T binding to amyloid fibrils. *Biochimica et Biophysica Acta (BBA) - Proteins and Proteomics* **1804**, 1405-1412 (2010).
35. K. Garai, C. Frieden, Quantitative analysis of the time course of Aβ oligomerization and subsequent growth steps using tetramethylrhodamine-labeled Aβ. *Proc. Natl. Acad. Sci. U. S. A.* **110**, 3321-3326 (2013).
36. J.-X. Lu *et al.*, Molecular structure of β-amyloid fibrils in Alzheimer's disease brain tissue. *Cell* **154**, 1257-1268 (2013).
37. R. Aleksis, F. Oleskovs, K. Jaudzems, J. Pahnke, H. Biverstål, Structural studies of amyloid-β peptides: Unlocking the mechanism of aggregation and the associated toxicity. *Biochimie* **140**, 176-192 (2017).
38. N. Schwierz, C. V. Frost, P. L. Geissler, M. Zacharias, From Aβ Filament to Fibril: Molecular Mechanism of Surface-Activated Secondary Nucleation from All-Atom MD Simulations. *J. Phys. Chem. B* **121**, 671-682 (2017).
39. M. Tö *et al.*, Secondary nucleation in amyloid formation. *Chem. Commun.*, (2018).
40. F. A. Aprile *et al.*, Selective targeting of primary and secondary nucleation pathways in Aβ42 aggregation using a rational antibody scanning method. *Science Advances* **3**, e1700488 (2017).
41. W. Qiang, W.-M. Yau, Y. Luo, M. P. Mattson, R. Tycko, Antiparallel β-sheet architecture in Iowa-mutant β-amyloid fibrils. *Proc. Natl. Acad. Sci. U. S. A.* **109**, 4443-4448 (2012).
42. D. P. Smith *et al.*, Trifluoromethyldiazirine: an effective photo-induced cross-linking probe for exploring amyloid formation. *Chem. Commun.*, 5728-5730 (2008).
43. D. M. Walsh *et al.*, A facile method for expression and purification of the Alzheimer's disease-associated amyloid β-peptide. *FEBS J.* **276**, 1266-1281 (2009).
44. K. L. Stewart, E. Hughes, E. A. Yates, D. A. Middleton, S. E. Radford, Molecular Origins of the Compatibility between Glycosaminoglycans and Aβ40 Amyloid Fibrils. *J. Mol. Biol.* **429**, 2449-2462 (2017).
45. M. Cheon, I. Chang, C. K. Hall, Extending the PRIME Model for Protein Aggregation to All Twenty Amino Acids. *Proteins* **78**, 2950-2960 (2010).
46. M. Cheon, C. K. Hall, I. Chang, Structural Conversion of $A\beta_{17–42}$ Peptides from Disordered Oligomers to U-Shape Protofilaments via Multiple Kinetic Pathways. *PLoS Comput Biol* **11**, e1004258 (2015).
47. M. Cheon, I. Chang, C. K. Hall, Influence of temperature on formation of perfect tau fragment fibrils using PRIME20/DMD simulations. *Protein Sci.* **21**, 1514-1527 (2012).

Acknowledgments

General: We thank Dr Matt Iadanza for help with taking and processing the EM images. We also thank Nasir Khan for excellent technical support and members of our laboratories for excellent discussions during the course of the work.

Funding: This work was supported by National Institutes of Health Grants R01 EB006006 and in part by National Science Foundation (NSF) Research Triangle Materials Research Science and Engineering Centers (MRSEC) Grant DMR-1121107 and by NSF grant CBET 581606 and by EPSRC grants EP/N035267/1, EP/N013573/1 and EP/KO39292/1. SER acknowledges funding from the ERC (grant agreement number 322408) and the Wellcome Trust (204963). SJB gratefully acknowledges BBSRC for a PhD studentship grant BB/J014443/1. The EM was purchased with funding from Wellcome Trust (108466/Z/15/Z) and

(094232/Z/10/Z). YW and CKH gratefully acknowledge the support of a Cheney Visiting Scholar Fellowship from University of Leeds.

Author contributions: SJB performed the experimental work; YW performed simulations; KLS performed expression and purification of $A\beta_{40}$; SER, CKH and AJW designed the research; SJB, YW, AEA SER, CKH and AJW wrote the paper.

Competing Interests: The authors declare that they have no competing interests

Figures and Tables

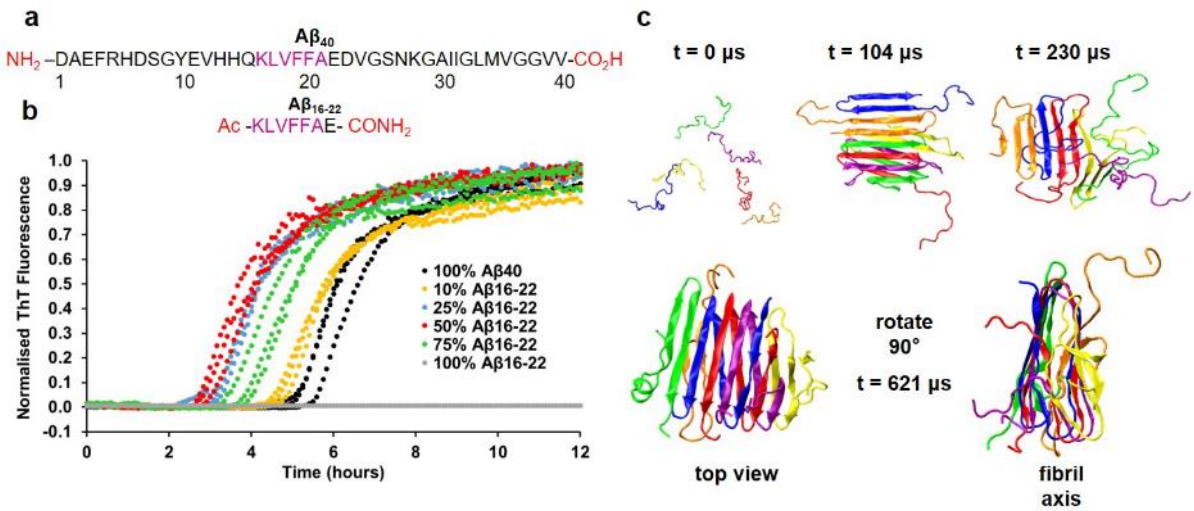

Figure 1. **Co-aggregation of $A\beta_{16-22}$ and $A\beta_{40}$ results in accelerated aggregation kinetics for $A\beta_{40}$** (a) The primary sequence of $A\beta_{16-22}$ and $A\beta_{40}$, including the groups at each termini. The central rcognition motif KLVFF is highlighted in purple. (b) ThT fluorescence assays showing that the aggregation rate of $A\beta_{40}$ increases as the ratio of $A\beta_{16-22}$ to $A\beta_{40}$ is increased (with the total peptide concentration held constant at 40 μM). (c) Simulation snapshots of the aggregation of six $A\beta_{40}$ monomers into a β-sheet rich hexamer at an $A\beta_{40}$ concentration of 5 mM. At the start of the simulation (0 μs) all the peptides are in random coils but as the simulation progresses they aggregate into antiparallel, in-register β-sheets (104 μs). This oligomer then unfolds, losing some of its β-sheet structure (230 μs) prior to a rearrangement in which the β-sheets rearrange, forming a stable fibril with each $A\beta_{40}$ peptide containing three β-strands (621 μs) engaged in parallel intermolecular hydrogen-bonding.

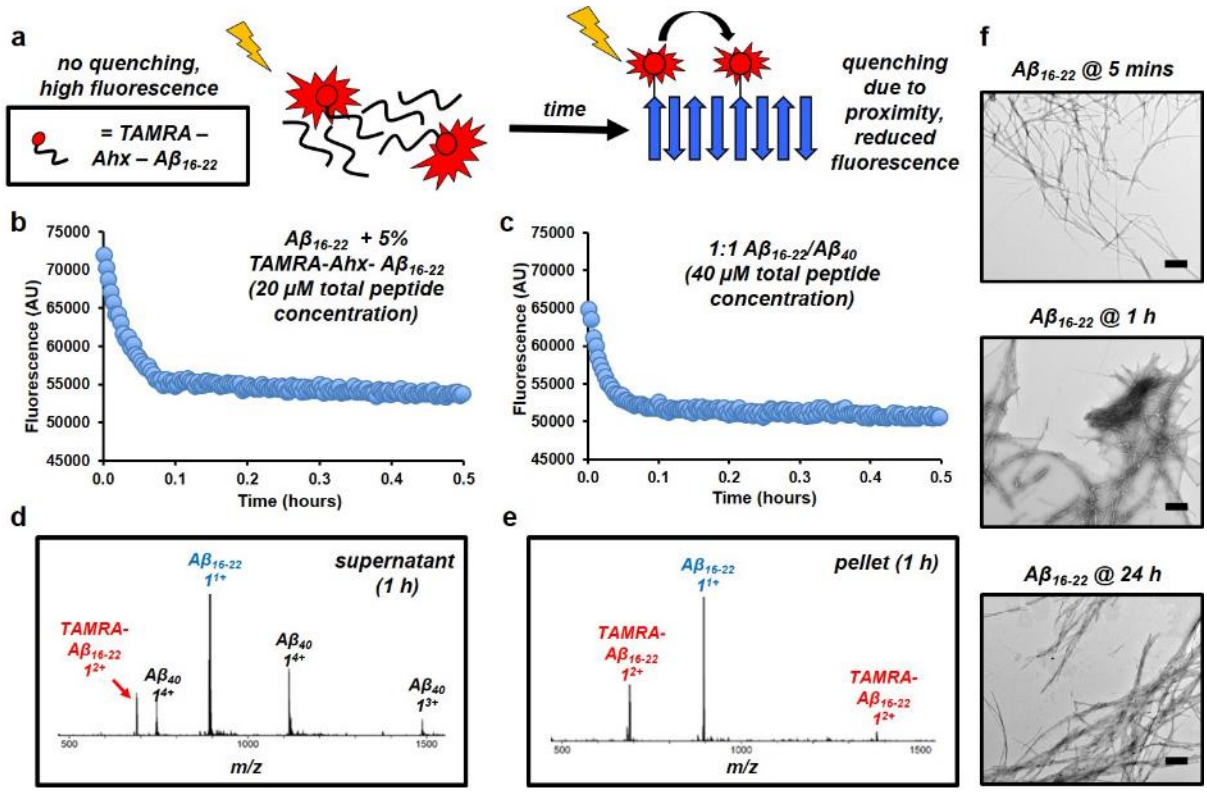

Figure 2. **Aggregation kinetics of $A\beta_{16-22}$ are unaffected by the presence of $A\beta_{40}$**. (a) Schematic showing the principle behind the fluorescence quenching assay used to determine the aggregation rate of $A\beta_{16-22}$. (b) As self-assembly occurs, the TAMRA-labelled peptides (40 μM, total peptide, containing 5% (w/w) TAMRA-Ahx-$A\beta_{16-22}$) are sequestered into the fibril structure. This brings the fluorophores into proximity, resulting in fluorescence quenching. (c) Aggregation of $A\beta_{16-22}$ (containing 5% (w/w) TAMRA-Ahx-$A\beta_{16-22}$) and $A\beta_{40}$ at a 1:1 mol/mol ratio (total peptide concentration 40 μM). A single transient is shown that is the median of 3 replicates measured. (d, e) Sedimentation and separation of the pellet and supernatant of the 1:1 mixed system and analysis of the fractions using ESI-MS after 1 h indicates that $A\beta_{40}$ is present in the (d) supernatant and only very small amounts within the (e) pellet. (f) Under these conditions, fibrils of $A\beta_{16-22}$ are present after 5 mins incubation. Scale bar: 500 nm.

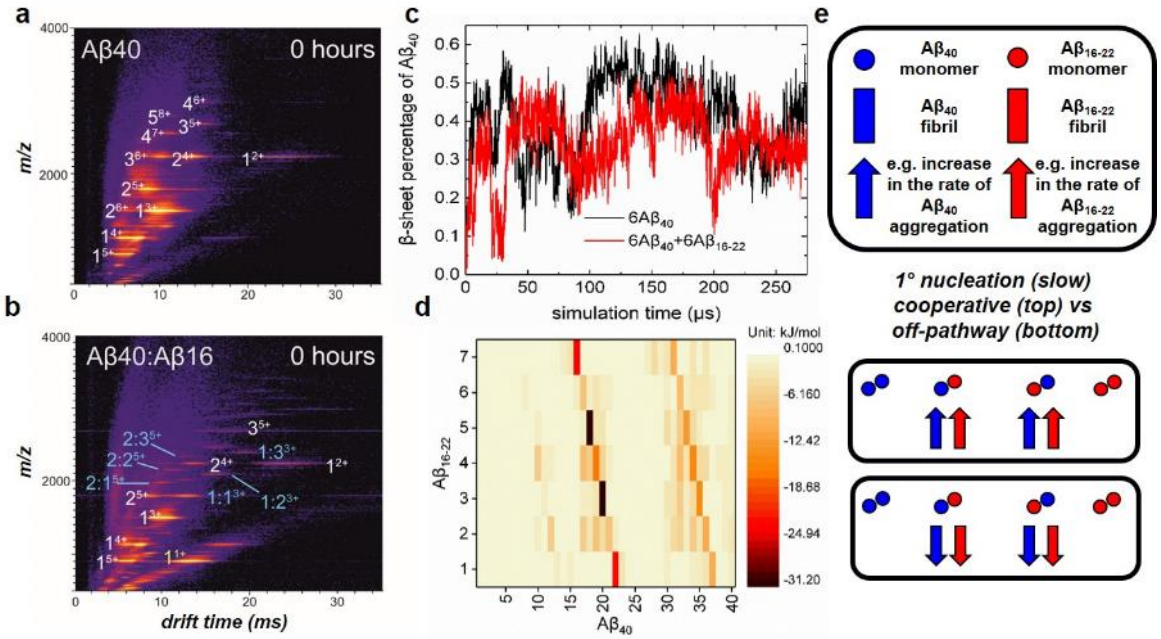

Figure 3. **$A\beta_{16-22}$ can interact with $A\beta_{40}$ monomers and dimers**. (a) Native ESI-IMS-MS drift-scope images of $A\beta_{40}$ indicate the presence of multiple oligomeric species of $A\beta_{40}$ (white numbers). (b) When mixed at a 1:1 mol/mol ratio with $A\beta_{16-22}$ (yellow numbers) a number of heteromeric species are observed (light blue numbers) immediately following mixing. The oligomer size is given (1, 2, 3 etc) with the charge state in superscript. (c) DMD simulation showing the percent β-sheet formed by $A\beta_{40}$ during aggregation in the absence (black) or presence (red) of $A\beta_{16-22}$. (d) Energy contact map between one monomer of $A\beta_{16-22}$ and one of $A\beta_{40}$ scaled by energy (bar shown alongside) showing that residues 17-20 (LVFF) and 31-34 (IIGL) form the strongest interactions. (e) Co-aggregation can have differing effects on the 1° nucleation of each peptide, depending on whether the mixed oligomers formed can progress to form mixed fibrils or are off-pathway and take no further part in the aggregation reaction. Circles represent monomers and blocks represent fibrils, with $A\beta_{16-22}/A\beta_{40}$ in red and blue respectively. Adapted from (35).

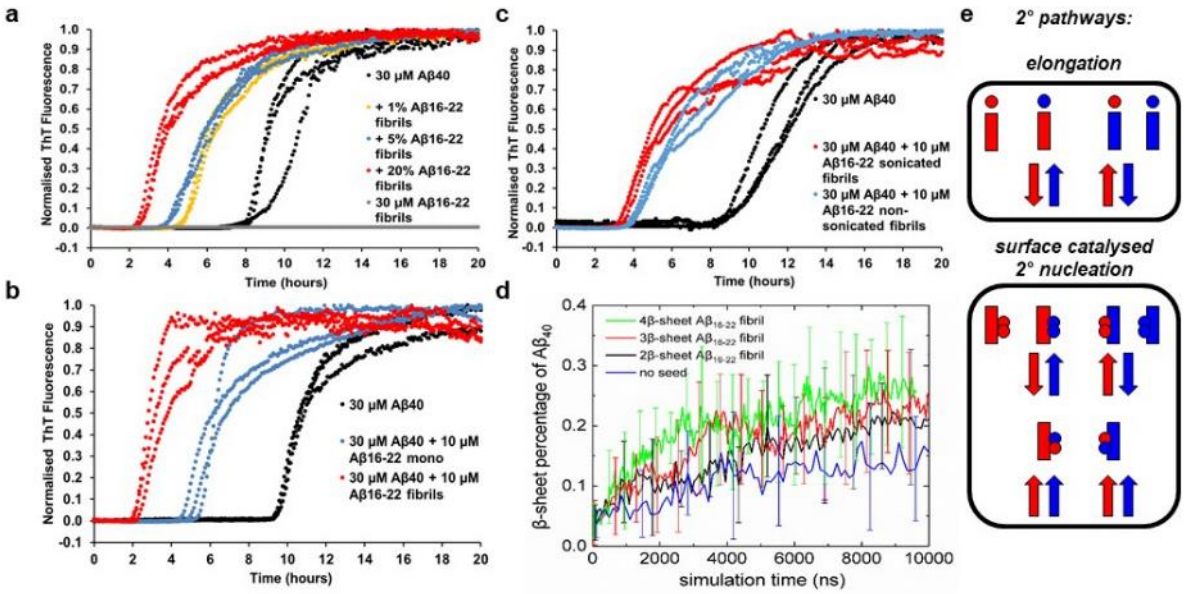

Figure 4. **$A\beta_{16-22}$ fibrils increase the aggregation rate of $A\beta_{40}$ to a greater extent than $A\beta_{16-22}$ monomers.** (a) Increased concentrations (% w/w) of $A\beta_{16-22}$ fibrils were added to $A\beta_{40}$ monomers (as shown in the key) and the aggregation rate measured by ThT fluorescence. (b) Direct comparison of the effect of $A\beta_{16-22}$ monomers (i.e. taken straight from a DMSO stock) and $A\beta_{16-22}$ fibrils on $A\beta_{40}$ aggregation. (c) Effect of sonicating the $A\beta_{16-22}$ fibrils on $A\beta_{40}$ aggregation rate shows little effect compared with the data shown in (a) (see text for details). (d) Plots of the percent β-sheet formed by $A\beta_{40}$ in the absence (blue) or presence of preformed 2 (black), 3 (red) or 4 (green) β-sheet $A\beta_{16-22}$, determined using DMD, showing that an increased $A\beta_{16-22}$ fibril size increases the rate of $A\beta_{40}$ aggregation. (e) During co-aggregation experiments both elongation and surface catalysed mechanisms can occur, each has a different effect on the rate of assembly of each peptide (the same notation is used as in Fig. 3e, with circles representing monomers, blocks fibrils and $A\beta_{16-22}$/$A\beta_{40}$ in red and blue, respectively). Adapted from (35).

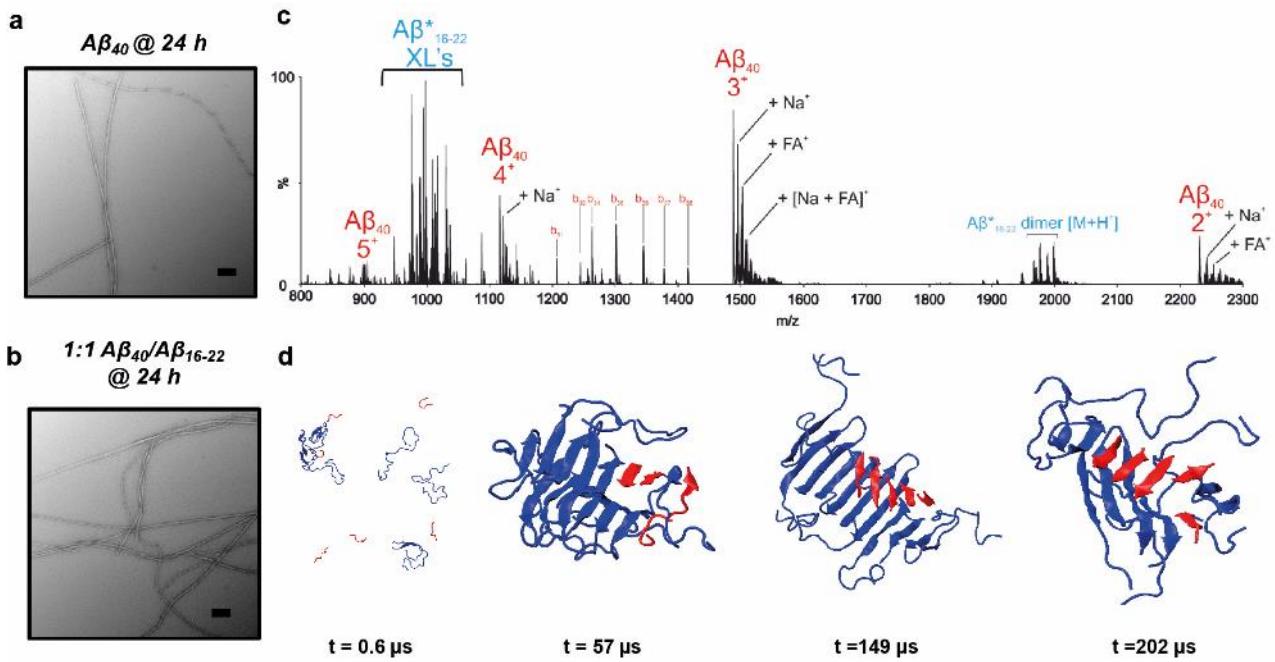

Figure 5. **Aβ16-22 and Aβ40 do not co-assemble during co-aggregation.** Negative stain TEM analysis of $A\beta_{40}$ incubated for 24 h in the (a) absence or (b) presence of $A\beta_{16-22}$. Scale bar = 200 nm. (c) PIC of mixtures of diazirine labelled $A\beta_{16-22}$ ($A\beta^*_{16-22}$) and $A\beta_{40}$ incubated for 24 h and then irradiated for 30 s. Only homomolecular $A\beta_{16-22}$ cross-links are observed, indicating that the fibrils are not co-polymerised at the end of the reaction (the inset depicts the mechanism of PIC of the diazirine group. (d) DMD simulation snapshots of co-aggregation of $A\beta_{40}$ (blue) and $A\beta_{16-22}$ (red) indicate that separate homomolecular oligomers are formed at t = 202 μs.

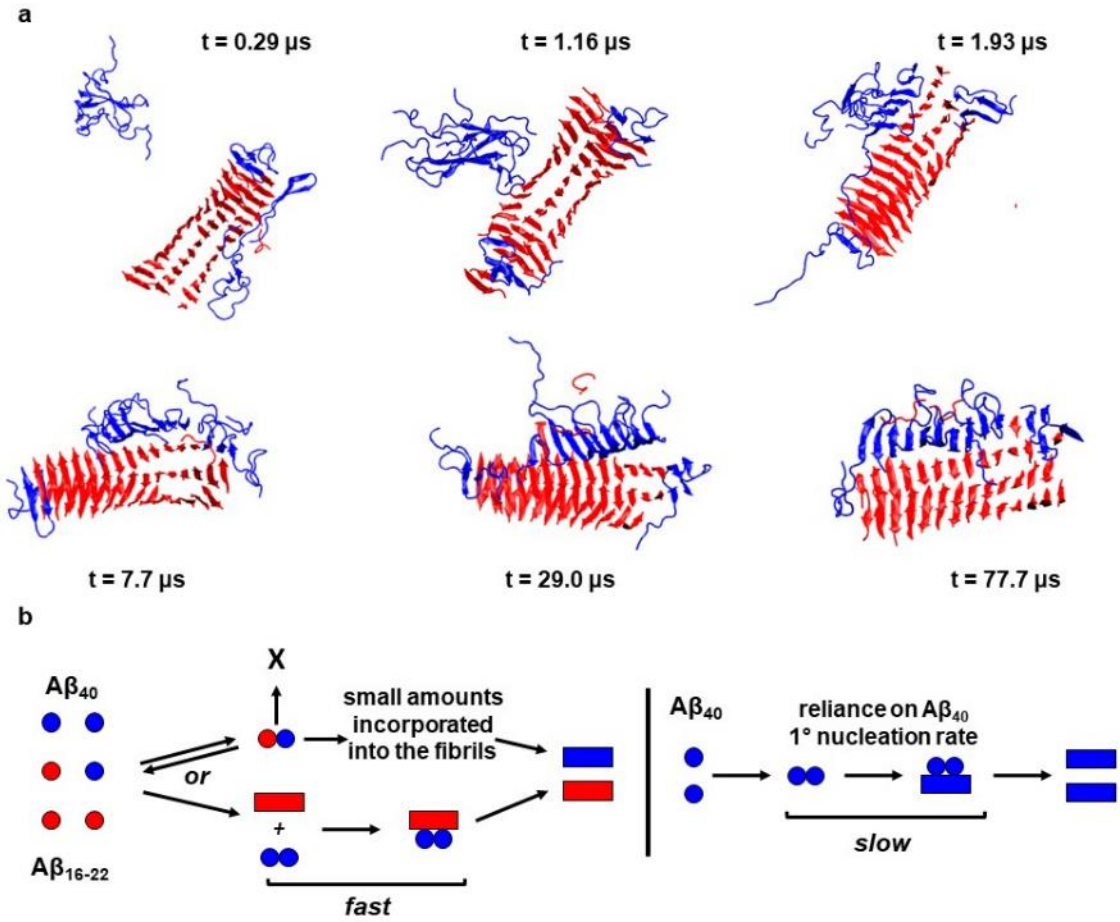

Figure 6. **$A\beta_{16-22}$ fibrils catalyse $A\beta_{40}$ assembly through secondary surface nucleation.** (a) Simulation snapshots of the process by which $A\beta_{16-22}$ fibrils (red) increase the aggregation rate of $A\beta_{40}$ (blue) through a surface catalysed 2° nucleation. (b) A schematic description of the mechanism is also included with $A\beta_{40}$ in blue and $A\beta_{16-22}$ in red.